Hao, W, Bashir, M, Li, C and Sun, C

 Flow control for high-solidity vertical axis wind turbine based on adaptive flap

http://researchonline.ljmu.ac.uk/id/eprint/15654/

Article

1   **Flow control for high-solidity vertical axis wind turbine based on Adaptive flap**

2   Wenxing Hao[a,*], Musa Bashir[b], Chun Li[c,*] and Chengda Sun[a]

3   [a] *School of Mechanical and Electrical Engineering, Shaoxing University, Shaoxing 312000, P.R.*

4   *China*

5   [b] *Liverpool Logistics, Offshore and Marine Research Institute, Liverpool John Moores University,*

6   *Liverpool, L3 3AF, United Kingdom*

7   [c] *School of Energy and Power Engineering, University of Shanghai for Science and Technology,*

8   *Shanghai, 200093, P.R. China*

9   **Abstract：** Adaptive flap as a new flow control technique with adaptability to the changing flow

10   separation has recently attracted much attention. This study uses the adaptive flap to mitigate the

11   flow separation of a vertical axis wind turbine with a high solidity of 0.75 and investigate its

12   performance and flow control mechanism by considering different flap lengths and locations. The

13   fluid flow is simulated using computational fluid dynamics with the shear-stress transport k-ω model,

14   and the flap motion is calculated based on the fluid-solid interaction methodology. The results show

15   that the flap can be adaptively raised by the backflow caused by flow separation and used to block

16   the backflow. The blocking of the backflow alleviates the flow separation problem and increases the

17   blades' aerodynamic torque. However, the long flap causes a negative effect due to its inability to

18   retract timely when the flow tends to the attached state at high tip speed ratio scenario. It is observed

19   that the short flap can avoid this problem when it is located far from the blade leading edge. Also,

20   the short flap located closer to the blade leading edge performs better at low tip speed ratios, even

21   though the performance is observed to be weakened by the trailing edge vortices suppressing the

1 flap from deployment. This study provides a technical approach and theoretical basis for better

2 alleviating the flow separation problems in vertical axis wind turbine.

3 **Keywords:** Vertical Axis Wind Turbine; Flow Separation Control; Adaptive Flap; Computational

4 Fluid Dynamics; Fluid-Solid Interaction

Nomenclature		M_S	Artificial reverse torque
c	Blade chord length	F_L	Lift force of the blade
R	Radius of the wind turbine	F_D	Drag force of the blade
h	Blade spanwise length	F_t	Blade tangent force to the trajectory
N	Blade number of the wind turbine	F_n	Blade perpendicular force to the
σ	Solidity of the wind turbine		trajectory
l_d	Flap location (distance from the hinge	λ	Tip speed ratio
	to the leading edge)	C_P	Power coefficient
l_f	Flap length	**Abbreviations**	
I_s	Moment of inertia of the flap	VAWT	Vertical Axis Wind Turbine
α	Angle of attack for blades	CFD	Computational Fluid Dynamics
φ	Blade azimuth angle	FSI	Fluid-Solid Interaction
ω	Rotation speed of the wind turbine	TSR	Tip Speed Ratio
θ	Flap angle	AoA	Angle of Attack
V	Inlet free stream velocity	RANS	Reynolds-Averaged Navier-Stokes
V_{rel}	Relative inflow wind speed for blade	BLE	Blade Leading Edge
M_f	Aerodynamic moment of the flap	BTE	Blade Trailing Edge

5 **1. Introduction**

6 　　Distributed wind power systems are mostly suitable for developing small-scale wind power

7 projects in populated and urban areas where convenience for power integration into exiting grids

8 and accessibility to end-users are the main attractions. Given the complexity and turbulent nature of

9 wind condition in urban areas and people's demand for a quiet living environment, the vertical axis

10 wind turbine (VAWT), shown in Fig.1, offers prominent advantages that include insensitivity to

11 wind direction and low level of noise generation [1]. However, VAWTs typically encounter a

12 challenging problem of low aerodynamic efficiency caused by the flow separation on the blades [2].

13 Flow separation generally occurs when the blade's angle of attack (AoA) undergoes a large periodic

1 variation at small tip speed ratios (TSR) and results in a reduction in lift to drag ratio of blade, thus,

2 decreasing the aerodynamic efficiency of VAWT [3]. In addition, vortex shedding generated by flow

3 separation also leads to unstable loads on the local blade and the downstream blades.

4

5 Fig. 1. Real scene of an H-type Darrieus VAWT

6 The flow separation problems in VAWTs can be alleviated by maintaining the AoA within a

7 safe range that generally does not exceed the stall angle of the blade during the rotation. An early

8 solution to this type of problem in VAWTs was developed based on a variable pitch system [4].

9 However, the variable pitch system is incapable of rapidly responding to the changing relative wind

10 velocity of VAWTs. The continuous reciprocating action of the variable pitch mechanism also

11 brings some challenges to the reliability of VAWTs [5]. Applications of flow control technologies are

12 generally more attractive in slowing down the flow separation in VAWTs because of simplification

13 of their local control and efficient response. The technologies are usually classified into two main

14 control strategies: passive and active [6]. Unlike the active control, passive control techniques do not

1 require external power supply and are therefore more suitable for small VAWTs. Yan et al. [7]

2 studied the flow control effect of the vortex generators on a VAWT and concluded that the use of

3 vortex generators in VAWTs improve the aerodynamic efficiency only when the flow separation

4 itself is weak. This implies that the performance of vortex generators is not apparent at low TSR

5 conditions in which extensive flow separation occurs. Wang et al. [8] used the blade leading-edge

6 serrations to mitigate the flow separation in a VAWT. The results show that the maximum increase

7 in the power coefficient is around 18.7% at a TSR of 2.0. However, the performance of the

8 leading-edge serrations gradually decreases when the working condition deviates from the range of

9 TSR 1.5 ~ 2.5. Mohamed et al. [9] investigated a VAWT with slotted blades that promote flow

10 attachment by providing a jet. It is found that the slotted blades had a significantly positive effect in

11 mitigating flow separation at low TSRs. Meanwhile, a negative effect is induced by the slotted

12 blades under high TSR conditions.

13   The above conventional passive control technologies promote the flow attachment (i.e.

14 mitigate the flow separation) mainly by enhancing the kinetic energy of the fluid in the boundary

15 layer by altering local shape of the blade to form disturbance. As the flow regime of the VAWT

16 changes periodically from attached flow to different degrees of separated flow and then to

17 reattachment flow, the aerodynamic performance of blades will be reduced in the attached flow

18 phase due to changes in the blade shape. In addition, the passive control technologies in this

19 scenario are difficult to adapt to the condition with different degrees of flow separation due to its

20 shape limitation.

21   In order to overcome these drawbacks, the control system needs to be designed to adapt itself

1   to all types of flow conditions. The design of such a self-adapting mechanism is inspired by flight

2   dynamics of birds. It has been observed that when some birds are dealing with gusts or flying at

3   low speed, the feathers on the upper surface of their wings are raised. The raising of these feathers

4   are caused by the wind flow separation backflow and then used to block the backflow, resulting in

5   reduced flow separation to provide enough lift for the flight [10]. Consequently, in order to take

6   advantage of this phenomenon, an adaptive flap was proposed as a rigid or flexible sheet hinged on

7   the leeward side of the blade, as shown in Fig. 2 [11]. Ideally, when flow separation occurs, the flap

8   is raised to a position that is adaptive to the flow condition in order to implement flow control.

9   Equally, when flow is attached to the blade surface, the flap keeps the attached state in order to

10   maintain the original shape of the blade. The flap rotates adaptively under the driving force of the

11   fluid without control system or power consumption and is considered to be more suitable in

12   alleviating the complex flow separation problems of the VAWT.

A: Low-pressure   B: High-pressure
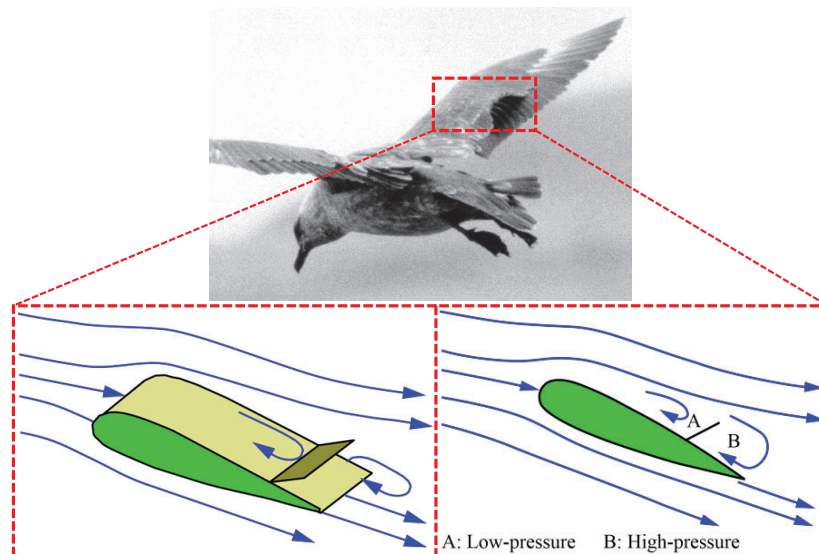
13

14   Fig. 2. Schematic diagram of adaptive flap derived from the feathers rising phenomenon on bird

15   wing [11]

1   As a new passive control technology, adaptive flap has been studied systematically since 1996

2   [12]. Initially, a flight experiment with flaps installed on the wings of an aircraft was conducted by

3   Bechert et al. [10]. About 11.4% increase in maximum lift for the blade by the flaps was observed in

4   the flight test, allowing the aircraft to fly at a lower speed with favorable handling of the glide in

5   dynamic stall condition. A more detailed experimental study about the adaptive flap was carried out

6   by Bramesfeld et al. [13] to explain the control mechanism. The results show that the adaptive flap

7   increased the blade lift by 20% with a discontinuity of the blade surface pressure at the flap hinge.

8   The pressure discontinuity resulted in a decrease of upstream pressure and an increase of

9   downstream and lower-surface pressure, contributing to the lift increase. In terms of the flap

10   configuration, Kernstine et al [14] pointed out that the flap length within a range of 10% ~ 40% of

11   the blade chord length is appropriate. It should be noted that a longer flap will cause premature

12   deployment at low AoA. The results of Allemand et al [15] show that the flap near the blade leading

13   edge (BLE) offers a more positive effect on deep stall than the trailing edge. In addition, Wang et al.

14   [16] and Arivoli et al. [17] carried out flap studies based on the blades with different aspect ratios and

15   confirmed that the performance of the flap was slightly reduced by the tip loss of the blade with a

16   low aspect ratio. It is worth noting that Meyer et al. [11] and Schatz et al. [18] highlighted that the flap

17   does not yield an optimal performance at aerodynamic equilibrium position, resulting in the lift

18   force of about 5% lower than that of the optimal position. Hao et al. [19] clarified the flap optimum

19   operating conditions and based on this, proposed two methods to constrain the flap to work at the

20   optimal position.

21   Although the above studies have attempted to confirm the advantages and application prospects

1   of the flap for flow separation control, their findings are mostly based on simple flow condition and

2   the dynamic effect of the flap has been not fully explored yet. More specifically, the effect of the

3   flap in an actual mechanical equipment such as a VAWT which are known to have complex flow

4   separation problems is still unclear. Although Hao et al. [19] are the early pioneers in the conduct of

5   a preliminary study on adaptive flap application in VAWT, only one flap configuration was

6   investigated in their studies. To date, a comprehensive research on the flow control of the adaptive

7   flap in a VAWT considering different flap configurations is still required. In continuation of work in

8   ref. [19], the present work examines different flap configuration parameters including geometry,

9   location, and installation on both the inner and outer sides of the blade to comprehensively

10   investigate the performance of the adaptive flap, predict its optimal parameters and to explore the

11   flow control process. A high-solidity VAWT is selected for this study. Compared with the

12   low-solidity VAWT, the high-solidity VAWT has a larger blade chord that can reduce the

13   degradation of blade performance caused by turbulence [20], but when the TSR deviates from the

14   optimal value in a decreasing manner, the fluctuation range of the AoA increases at a faster rate and

15   the flow separation becomes very rapid [21]. Consequently, the flow separation of the high-solidity

16   VAWT deserves more attention.

17   In this paper, for one configuration, the adaptive flaps are simultaneously installed on the

18   high-solidity VAWT in a way of one flap to one side of the blades. By considering different flap

19   configurations, the performance of the flap is systematically studied using computational fluid

20   dynamics (CFD) combined with fluid-solid interaction (FSI) methodology. More specifically, the

21   flaps are firstly installed on the inner sides of the blades in order to study the influence of the flap

1   length and flap location on the flap performance at different TSRs. Then, the performance of the

2   flaps mounted on both sides of the blades is investigated and compared with the flaps installed on

3   the inner side of the blades only. Finally, the control mechanism of the flap is analyzed and its

4   advantage and weakness are discussed. The main contributions of this study are summarized as

5   follows:

6   1. Adaptive flap for application as a flow control system on VAWT is developed formally for the

7   first time. The new concept offers the advantage of being able to self-adapt to different flow field

8   conditions in order to handle the complex flow separation problems that exist in VAWTs. This is

9   in direct contrast to the existing (traditional) flow control techniques that are incapable of adapting

10   to any changes in flow fields.

11 2. Following a comprehensive and systematic investigation on configurations of the new adaptive

12   flap on a VAWT, it's geometric and location parameters have been considered in order to enhance

13   the understanding of its physical and mechanical behaviours. In addition, geometry and location

14   of the adaptive flap installed on a VAWT that offer the optimum performance have been

15   identified.

16 3. The results of this study confirm the inherent advantages and reveal the weaknesses offered by the

17   adaptive flap in flow control of a VAWT. It can lay the theoretical foundation for the practical

18   application of the adaptive flap in VAWTs.

19   Following the introduction, the computational methods used in the study are presented in

20 Section 2. This section also describes the geometry and operational parameters of the flap and

21 VAWT. Moreover, the verification and validation studies are presented to confirm the appropriate

1　time step size and grids number required by credible simulations to the flow control problems of the

2　high solidity VAWT. Results obtained from this study are reported in Section 3. Discussions of the

3　results are presented in Section 4, while the conclusions are presented in Section 5.

4　**2. Methods**

5　　This section introduces the geometry and model parameters of the flap and VAWT, and the

6　computational methods used to study the fluid flow control and their interactions with dynamic flap

7　system in VAWTs. The computational domain and grids distribution are also presented.

8　*2.1. Adaptive flap and vertical axis wind turbine models*

9　　Taking the installation of the flaps on the inner sides of the blades as an example, Fig. 3 shows

10　the model of the adaptive flap and the VAWT [22]. The adaptive flap is rigid and installed on the

11　NACA0018 airfoil blade with the flap shape fitting the blade surface. The flap rotates around the

12　hinge point S under the fluid drive. A groove is introduced on the blade surface to facilitate the

13　flap's retraction and avoid changing of the blade's original shape during attached flow scenario. The

14　trailing edge of the flap is designed to bend outward slightly, so that it can cause the flap to adhere

15　to the blade surface in a stable manner when it is under the impact of attached flow. Since the

16　bending range and deflection angle shown in Fig.3 are very small, no evidence of obvious

17　disturbance to the attached flow was observed. The flap location is expressed as the distance from

18　the hinge point to the BLE and denoted by the symbol l_d. The flap length is denoted by l_f. The

19　symbol θ represents the flap angle, which is limited to $0° \sim 72°$. The upper limit is introduced to

20　prevent the flap from overturning and thus losing its effectiveness. In the calculation process, when

21　the flap angle exceeds the range, it will be subjected to an artificial reverse torque causing it to

1   return to the effective range.
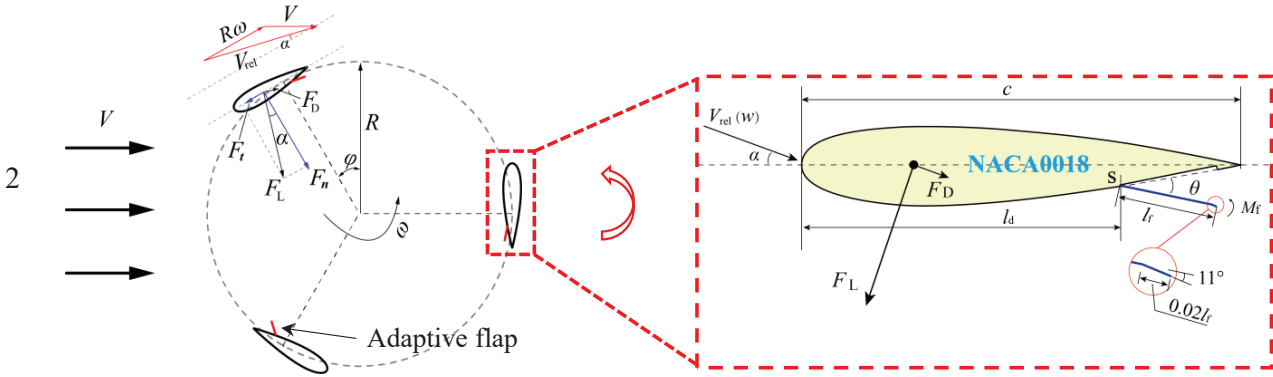
3   Fig. 3. VAWT with the adaptive flaps

4   It should be noted that the flap in Ref. [19] is driven by a composite torque related to the flap

5   surface pressure, which offers a better performance than that of a free rotation directly driven by the

6   fluid. However, the free rotation is based on a more basic concept and is the easiest way to achieve

7   the rotation. Therefore, the flap used in this study is set to rotate freely. The aerodynamic moment

8   due to the air flow over the flap is denoted as M_f. The artificial reverse torque is denoted as M_S. The

9   equation of motion of the rigid flap is expressed by Equation (1).

10       $$I_S \cdot \frac{d^2\theta}{dt^2} = M_f + M_S \qquad (1)$$

11   where the I_S is the moment of inertia determined by the assumption that the flap is made of a

12   cellulose acetate sheet with a density of 1400 kg/m^3 and a thickness of 0.3mm.

13   For the VAWT, φ is the blade azimuth angle, and ω is the rotational speed. The aerodynamic

14   lift F_L and drag F_D on the blade are combined into the tangential force F_t to drive the wind turbine

15   to rotate and generate power. The efficiency of wind turbine in obtaining wind energy can be

16   measured by the power coefficient, as shown in Equation (2).

17       $$C_P = \frac{NT\omega}{0.5\rho V^3 A} \qquad (2)$$

where N is the blade number, and T is the torque generated from one blade, i.e. $T = F_t R$; ρ is the air density, V is the incoming free stream velocity and A represents the windward area of the wind turbine rotor, where $A=2Rh$ and h is the span-wise length.

The specifications of the above geometry and operating parameters are shown in Table 1. The original VAWT model adopted in this paper comes from an experiment in Ref. [23]. The VAWT model has a high solidity ratio of 0.75. For comparison with the experiment, the operating parameters of the present VAWT are consistent with those in the reference. Among them, the inlet velocity is 8 m/s with the turbulence intensity of 0.8% and the turbulence length scale of 0.0028 m. Note that Flap 7520 indicates that the flap is located at l_d of $0.75c$ corresponding to the "75" in the number and has the flap length l_f of $0.20c$ corresponding to the "20" in the number. In the following sections, Flap 7510, Flap 5810, and Flap 4010 with the same naming rule will also be used.

Table 1. Geometry and operating parameters of the VAWT with the adaptive flaps

Items	Specifications	Items	Specifications
Airfoil	NACA0018	Solidity $\sigma=Nc/D$	0.75
Blade chord length c	0.2 m	Flap 7520	$l_d=0.75c$; $l_f=0.20c$
Rotor diameter D (2R)	0.8 m	Inlet velocity V	8 m/s
Rotor length h	1 m	Rotational speed ω	12-30 rad/s
Blade number N	3	Tip speed ratio λ	0.6-1.5

Flaps with the same length and location were firstly installed on the inner sides of the blades (one flap on each side). The flap's performance is investigated by considering different flap lengths and locations. Then, Flap 7510 is installed symmetrically on both sides of the blades (two flaps per

1 each blade) in order to compare the performance improvements of the flap on the inner and outer

2 sides of the flow separation of the blade.

3 *2.2. Computational methods*

4 To calculate the flap motion, that is, the flap angular displacement at each time step in the FSI

5 process, Equation (1) is converted to Equation (3) for time stepping.

6 $$\theta^i = \theta^{i-1} + [\left(M_f^{\ i} + M_s^{\ i}\right)/I_S \times \Delta t + \left(\theta^{i-1} - \theta^{i-2}\right)/\Delta t] \times \Delta t \tag{3}$$

7 A flap motion solving module is developed within the User Defined Functions (UDF) of the

8 CFD software ANSYS Fluent. A schematic diagram of the FSI process is shown in Fig. 4. For the

9 FSI implementation, a strong coupling framework is adopted from Wang et al. [24]. More

10 specifically, the framework facilitates the interchange of data between the fluid and solid sides of

11 the system, which is performed through several rounds of iterations for each time step until the

12 convergence requirements are satisfied. It should be noted that flow field is adjudged to converge

13 once the aerodynamic torque residual of the wind turbine reduces to 10^{-5}, and the flap motion is

14 considered to converge when the flap angle residual reduces to 10^{-4}. The procedure for the FSI

15 process involved the following steps: First, the variables of the flow field are calculated using the

16 CFD method (i.e. ANSYS Fluent). Secondly, the aerodynamic force on the flap is extracted by

17 integrating the flap surface pressure and then used to calculate the flap angle using Equation (3).

18 Based on the predicted flap angle, the fluid-solid interface and the flow domain are updated

19 accordingly, in order to highlight the effectiveness of the flap on the flow field. It should be noted

20 that if the solution does not converge when the iteration exceeds the set number in a time step, the

21 data will be recorded as a reference for determining whether to reduce the time step and repeat the

1   process until convergence is attained.


```
                    ┌─────────────────┐
                    │  Initialization │
                    └─────────────────┘
                            │
        ┌ ─ ─ ─ ─ ─ ─ ─ ─ ─ ┼ ─ ─ ─ ─ ─ ─ ─ ─ ─ ┐
        │         ┌──────────────────┐
        │         │ Calculate the flow│
        │         │  field by CFD     │
        │         └──────────────────┘
        │                  │
        │         ┌──────────────────┐
i=i+1   │         │ Integrate the flap│   Iteration i      t=t+Δt
        │         │ surface pressure  │
        │         └──────────────────┘
        │                  │
        │         ┌──────────────────┐
        │         │  Solve the flap   │
        │         │     motion        │
        │         └──────────────────┘
        │                  │
        │      ┌────────────────────────┐
        │      │ Update the fluid-solid │
        │      │   interface and mesh   │
        │      └────────────────────────┘
        └ ─ ─ ─ ─ ─ ─ ─ ─ ─ ┼ ─ ─ ─ ─ ─ ─ ─ ─ ─ ┘
```

No $R \le R_{\lim} \parallel i \ge i_{\max}$ Yes $t \ge t_{\text{final}}$ No

Yes

Terminate the calculation
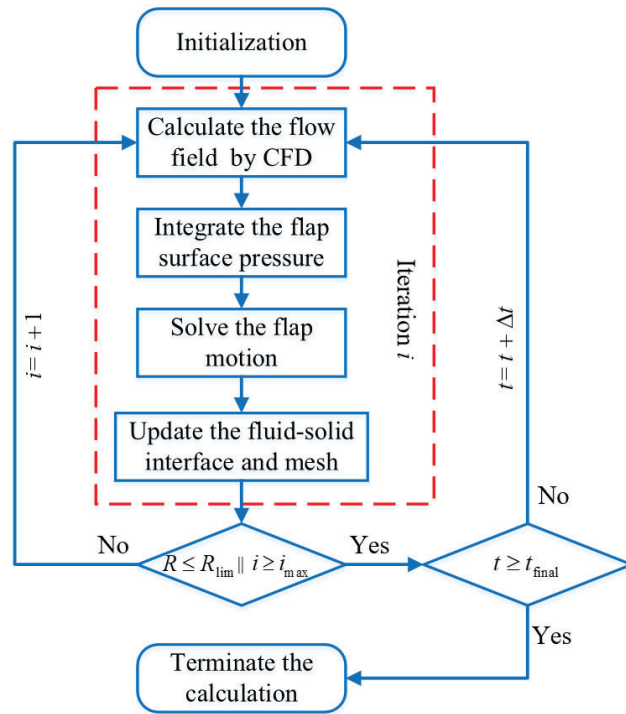
2

3   Fig. 4. Flowchart of the numerical solution process of the FSI

4   The Mach number in the flow field of wind turbines is generally below 0.3, this means that the

5   flow can be treated as incompressible [25]. Therefore, the fluid flow is governed by the

6   incompressible continuity equation and momentum equation known as Navier-Stokes equations.

7   The governing equations were discretized in the fluid domain using the finite volume method, and

8   the 2nd order discretization was used both in the temporal and spatial domains. The discrete

9   equations were solved using the pressure-velocity coupling method.

10   It is accepted that the 3D CFD model can produce more accurate aerodynamic prediction of

11   the VAWT due to its superior capability in accounting for the tip vortex and support rod compared

12   to the 2D model. However, updating the massive 3D mesh to cater for the rapid movement of the

13   flap is difficult and computationally inefficient. In addition, delay in mesh updating, which usually

1 occurs because the large deformation of the fluid-solid interface is hard to be absorbed quickly by

2 the 3D mesh, causes mesh updating failure. Therefore, the 2D model is adopted in this study

3 because it offers a better mesh deformability than the 3D model. In addition, the research of

4 Zanforlin et al. [26] pointed that when the aspect ratio (h/D) of VAWT exceeds 0.8, the deviation of

5 the power coefficient per span length does not exceed 6% within 70% of the blade in spanwise. The

6 present aspect ratio is 1.25, so we can believe that the dominant flow state changes very little along

7 the spanwise of the blade and has 2D characteristics, which provides support for the rationality of

8 using a 2D model to predict the dominant flow. For the 2D CFD model, the Reynolds-Averaged

9 Navier-Stokes (RANS) equations were adopted, and the turbulence fluctuation term is modeled

10 using the shear-stress transport (SST) k-ω model [27]. The SST k-ω model incorporates the

11 advantage of k-ω model [28] in dealing with boundary layer flow and the advantage of k-ε model [29]

12 in handling a free stream, making it suitable for the flow separation simulation [30].

13 *2.3. Computational domain and grid distribution*

14   The 2D computational domain and grid model are used in the calculation. The computational

15 domain and boundary conditions are shown in Fig. 5, which are identical to the settings proposed in

16 Ref. [19]. The computational domain is divided into an inner zone and an outer zone. The inner

17 zone rotates synchronously with the blades, exchanging data with the stationary outer zone through

18 the interface boundary. The synchronous rotation of the inner zone and the blades is adopted to

19 avoid the updating of the inner grids caused by the blade motion. The boundary condition on the

20 left side of the computational domain is the velocity inlet with the flow velocity of 8 m/s, where the

21 turbulence intensity is set as 3%, which is higher than the experimental value of 0.8% for it to make

1   up for the energy dissipation of the vortices moving from the inlet to the wind turbine. The

2   right-side boundary condition is the pressure outlet with a pressure value of the atmospheric

3   pressure (101.325 kPa). The upper and lower boundaries are both set as slip wall type, and the

4   remaining boundaries are all set as wall type.

5   The grid distribution of the computational domain is shown in Fig. 6 based on Flap 7520

6   model installed on the inner sides of the blades as an example. If flaps are installed on the outer

7   sides of the blades, the mesh near the flaps is similar to that of Flap 7520 model. In order to

8   facilitate the flap movement and mesh deformation, the flap is separated from the blade and rotates

9   around the hinge point (S point) shown in the figure. To model the sealing condition so that fluid do

10 not leak through the hinge in practice, the distance between the flap head and the blade is set at a

11 small value of $0.002c$. In addition, a "bulge part" is added to the inner side of the flap head in order

12 to prevent any potential fluid leakage.

13   The outer zone is made of fully orthogonal grids. The inner zone is divided by non-orthogonal

14 quadrilateral grids nested by several groups of grids. The flap not only moves around the center of

15 the wind turbine, but also rotates around its hinge point resulting in the change of the computational

16 domain. Therefore, the updating of grids near the flap is inevitable and the triangle grids are

17 adopted due to being easy to deform and reconstruct. During the flap rotation, the grids around the

18 flap deform first in the form of linearly elastic solid [31]. When the deformation causes the grids size

19 and skewness to exceed the limiting values, the local cell remeshing is applied for grid

20 reconstruction. In order to reduce the influence of grids updating on data transfer near the flap,

21 boundary layer grids on the flap surface are set to move synchronously with the flap.

1   Furthermore, more grids are distributed towards the BLEs, blade trailing edges (BTEs), and

2   the flaps by considering the gradient distribution of the flow field variables. To capture the

3   boundary layer flow near the wall, the SST k-ω model requires that the maximum y+ corresponding

4   to the height of first layer grids adjacent to the wall should not be greater than 3 [27]. Therefore, all

5   the wall type boundaries, except for the flap, are equipped with 20 layers of orthogonal grids with a

6   height of the first layer set at $10^{-4}c$ and a growth rate of 1.2. The orthogonal grids near the flap

7   surface have the same first layer height and growth rate as other wall type boundaries, but only 10

8   layers are arranged in order to transit smoothly to the triangular grids around them. The height of

9   the first layer grids is calculated based on the blade's Reynolds number estimated to be no more

10   than 2.7×10^5 according to the geometric dimension and operational parameters of the VAWT. Since

11   a higher Reynolds number requires a smaller height of the first layer grids, the height of the first

12   layer grids based on the highest Reynolds number satisfies the flow condition with a smaller

13   Reynolds number.

14   Keeping the above grids strategy and the wall normal dimensions of the boundary layer grids

15   unchanged, the following section will increase the global density of the grids in order to determine

16   the final number of the grids according to trial calculation results.
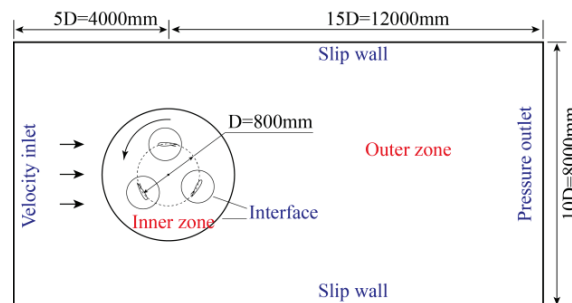
17

18   Fig. 5. Computational domain and boundary conditions [19]
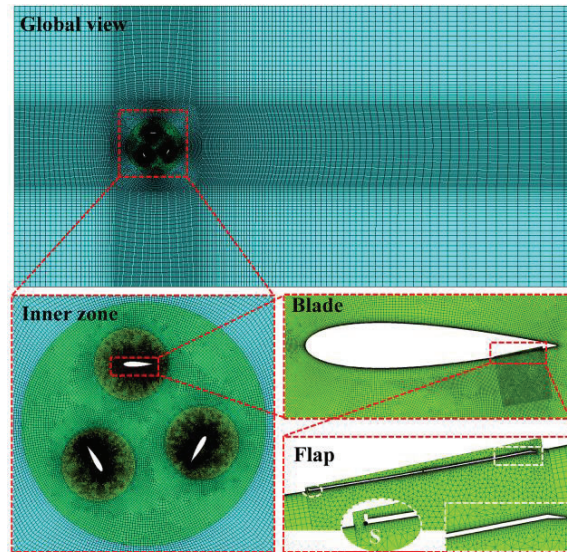
Fig. 6. Grids distribution in global and local view

2.4. Verification and validation of the computational model

This section presents the appropriate time step and grid numbers required to balance the computational requirements and resource consumption for the above calculation model. The numerical model is validated by comparisons against experimental results. It should be noted that the numerical model is a representation of the VAWT with Flap 7520 mounted on the inner sides of the blades. In addition, calculated results are extracted from the stable flow field after the wind turbine goes through certain revolutions and with the residual of average blade torque per revolution no more than 0.001. The power coefficient is generally evaluated in the form of its average value in a revolution. For convenience, all the power coefficients mentioned below refer to the average power coefficients.

2.4.1 Confirmation of the time step size and the grid numbers

In order to achieve a certain convergence accuracy, more accurate results require smaller time step. However, more computational resources are consumed in trying to fulfil this requirement.

1   Therefore, the appropriate time step needed for the simulation is confirmed by comparing the

2   power coefficients with different time steps on the premise that enough iterations per time step are

3   conducted and the residual reaches 10^{-5} for fluid flow and 10^{-4} for flap motion. In VAWT simulation,

4   the time step is usually represented by the blade azimuth increment per time step and the value of

5   0.5° was recommended by Rezaeiha et al. [32] and Edwards et al. [33]. Since the FSI process is more

6   complex, the time step is reduced and the corresponding power coefficients are calculated and

7   compared with each other. It is found that when the TSR is 1.2 or above, the blade azimuth

8   increments of 0.5° and 0.25° provide similar power coefficients. However, when the TSR is less

9   than 1.2, an obvious deviation between the power coefficients is observed. Nevertheless, the

10   azimuth increment of 0.125° gives similar results to that of the azimuth increment of 0.25° for all

11   the TSRs. Therefore, the azimuth increment per time step is set to 0.25° for the TSR less than 1.2

12   and 0.5° for the TSR of 1.2 or above.
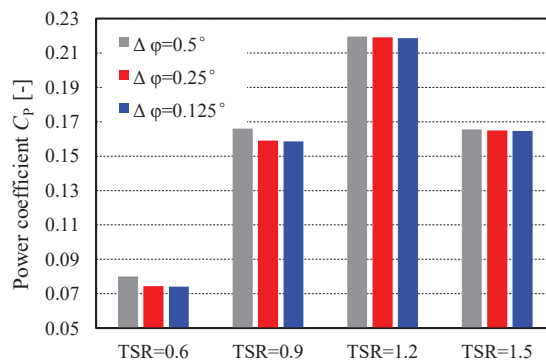
13

14   Fig. 7. Power coefficients variation with the azimuth increments at different TSRs

15   To confirm the appropriate grid numbers required for the simulations, three sets of grids were

16   established with the grid numbers of 143258, 185290, and 240949 respectively. When the mesh

17   changes from coarse mesh to fine mesh, the scale factor was used to control the mesh resolution.

1   This works by keeping the size gradient of the initial grids unchanged. When the scale factor

2   decreases, the grid sizes (except the grid heights of the boundary layers) at each position in the

3   computational domain decrease synchronously and maintain a linear relationship with the scale

4   factor. For the coarse mesh, medium mesh, and fine mesh in the present work, the scale factors are

5   1.0, 0.8, and 0.6 respectively. The single blade torque and the corresponding flap angle are both

6   used as indexes to evaluate the requirement of the grid numbers so as to give consideration to the

7   global grids and the grids near the flap. Fig. 8 shows the blade torques and flap angles with

8   different grid numbers varying with the blade azimuth. As can be seen from the plots, very similar

9   results are obtained from the medium and the fine grids, but significant deviations from the former

10   two are produced by the coarse grids, which is mainly reflected in the flap early deployment and the

11   larger flap angle. This indicates that the medium grids number should be adequate to calculate the

12   most dominant flow characteristics in VAWT and thus is used in the following simulation.

13
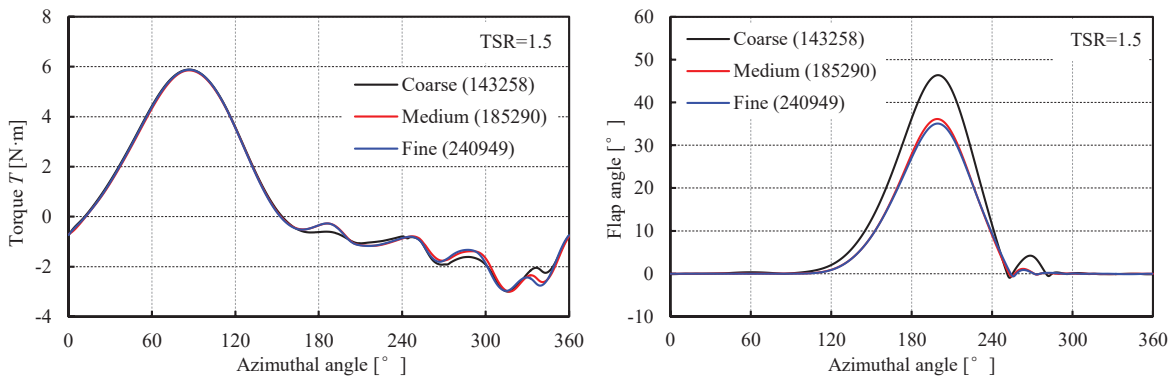
14   a. blade torques   b. flap angles

15   Fig. 8. Blade torques and flap angles varying with blade azimuth with different grid numbers

16   *2.4.2 Comparison between the numerical and experimental values*

17   The power coefficients of the VAWT with the clean blade are calculated and compared with the

1 experimental values from Ref. [23] and the 3D simulation results from Ref. [34] in order to verify

2 the reliability of the present model. The comparison is shown in Fig. 9. The computational results

3 for VAWT with the attached flap is added to explore the influence of the attached flap in

4 consideration that, although the attached flap fits the shape of the clean blade, there are still small

5 differences in the geometric and grid distribution nearby the flap comparing with the clean blade.

6 As can be seen from the plots, the simulation values of the clean blade and the attached flap are

7 very similar, indicating that the performance of the original blade is not affected by the flap

8 attached to the blade surface and the difference in the grid distribution can also be ignored.

9 Compared with the experimental values, the present values of the clean blade are higher with the

10 maximum values in excess of 16%, except at the TSR of 0.6 where it is slightly lower. This

11 exception may be due to the failure of the 2D model to consider the loss caused by the tip vortices

12 and support rods. In addition, Li et al [35] pointed out that the 2D RANS method generally has a

13 weak prediction on the flow separation. It should be noted that the support rods were also ignored

14 by the referenced 3D simulation based on the assumption that the support rods have a negligible

15 effect. As expected, the 3D simulation provided similar results with the experiment, showing that

16 the influence of the support rods is insignificant. Notwithstanding the preceding observation, the

17 deviation is within an acceptable range and the varying trend of the present power coefficient is

18 consistent with the experimental values. In combination with the comparison between the

19 simulation and experimental values of a single stationary airfoil with a rotating flap in Hao et al. [19],

20 it is concluded that the present study established a calculation model that is adequately capable of

21 meeting the research requirements.
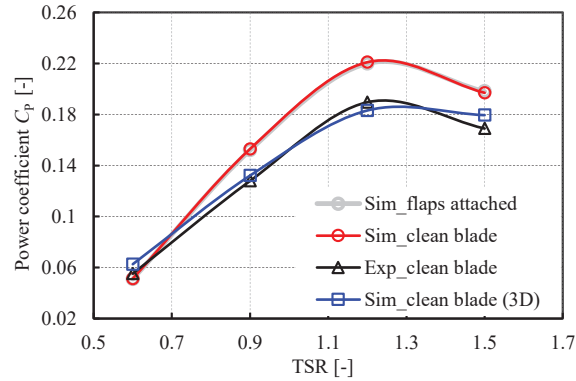
Fig. 9. Comparison between numerical and experimental values of power coefficient of the VAWT

3. Results

This section presents the results on the performance of adaptive flaps with different

configurations in mitigating the flow separation of the VAWT. The influence of adaptive flaps on

flow separation is reflected by the variations in the power coefficient of VAWT, blade aerodynamic

torque and flow-solid evolution.

3.1. Flow control effect of the flaps with different lengths

On the inner sides of the blades ($0.75c$ from the BLE), the flaps with a length of $0.2c$ (Flap

7520) and flaps with a length of $0.1c$ (Flap 7510) are installed respectively. The effects of the flaps

at different TSRs are studied. The power coefficients used to evaluate the flow control effects are

shown in Fig. 10. It can be seen that when the TSR is at 0.6 and 0.9, both types of flaps improve the

power coefficient, and the improvements are similar. The power coefficient at the TSR of 0.6 is

improved most significantly with an increased rate of about 45%. However, as the TSR increases,

the performance of the longer flaps is gradually weakened, and the flaps display a negative effect

that reduces the power coefficient at TSR of 1.5. Fortunately, the shorter flaps have an obviously

positive effect on the whole range of the TSRs. Fig. 11a shows the variations of the blade torques

1   with the azimuth angle at TSR of 1.5. It can be seen from the figure that the blade torque of Flap

2   7520 blade is significantly lower than that of the clean blade near the azimuth angles of 90°, 200°,

3   and 345°, leading to lower power coefficient of the VAWT with Flap 7520. For the shorter Flap

4   7510, the blade torque is higher than that of the clean blade at azimuth angle between 120° and

5   170°. Beyond this range, although the difference in torques between the flap blade and the clean

6   blade still exists, there is little difference in their average values.

7   To analyze the control mechanism of the adaptive flap and the cause of the negative effect by

8   the longer flap at TSR of 1.5, the variations in the flap angle are shown in Fig. 11b and the

9   evolutions of the flow field are shown in Fig. 12. From the variations in the flap angle, Flap 7520

10   starts to rise at an azimuth angle of about 120° and reaches the maximum flap angle of about 35° at

11   an azimuth angle of about 200°. This is followed by a complete retraction near the azimuth angle of

12   255°. Flap 7510 starts to deploy earlier near an azimuth angle of 30° than that of Flap 7520, and

13   reaches the maximum flap angle of 72° (the upper limit of the flap angle) near the azimuth angle of

14   130°. The retraction of Flap 7510 is also observed earlier and faster than that of Flap 7520. Due to

15   the fast retraction, the flap rebounded after a collision with the blade surface. It should be noted that

16   the flap collision process is simulated by adding the reverse torque.

17   From the flow field evolutions, as reflected by vorticity contours and relative velocity

18   streamlines at the key azimuth angles, the flow separation of the clean blade obviously appears near

19   the inner trailing edge at an azimuth angle of 120° and further develops at an azimuth angle of 150°.

20   Near the azimuth angle of 180°, the flow separation tends to the attached state, and at an azimuth

21   angle of 210°, where the flow inside of the blade is almost attached. For the longer Flap 7520, the

1 raising of the flap is not obvious until the azimuth angle of 150°. At the azimuth angle of 180°,

2 although the flap has been raised, it is still in the raising mode. From its interaction with the flow

3 shown by the streamlines, the raising flap has no obvious effect on the blocking of separation

4 backflow. Furthermore, at an azimuth angle of 210°, where the flow inner side of the blade tends to

5 the attached state, the flap obstructs the flow attachment and thus reduces the blade torque as shown

6 in Fig. 11a. For shorter Flap 7510, the flap has been raised at an azimuth angle of 120° and plays a

7 role in blocking the separation backflow with this phenomenon continuing until the azimuth angle

8 of 150°. Meanwhile, the blade torque is increased by Flap 7510 in this range. When the azimuth

9 angle reaches 180°, the streamline directions show that the shorter flap also slightly blocks the

10 mainstream flow, but the flap has almost fully retracted with the flow almost attached at an azimuth

11 angle of 210°. Compared with the flow field of the clean blade, the shorter flap did not cause

12 significant obstruction to the flow attachment.

13
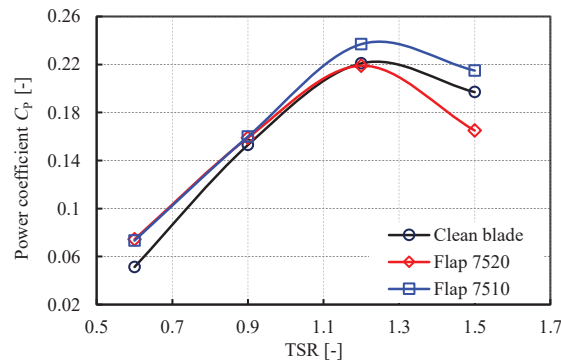
Fig. 10. Power coefficients of the VAWTs at different TSRs

14
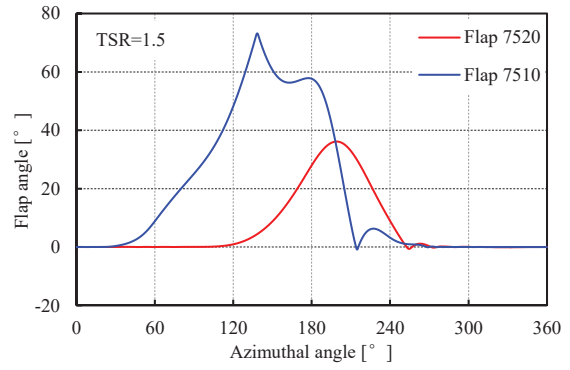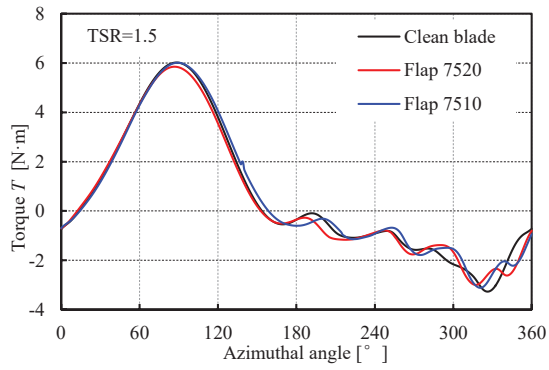
a. blade torques   b. flap angles

Fig. 11. Variations of the blade torques and flap angles with azimuth angle (TSR=1.5)
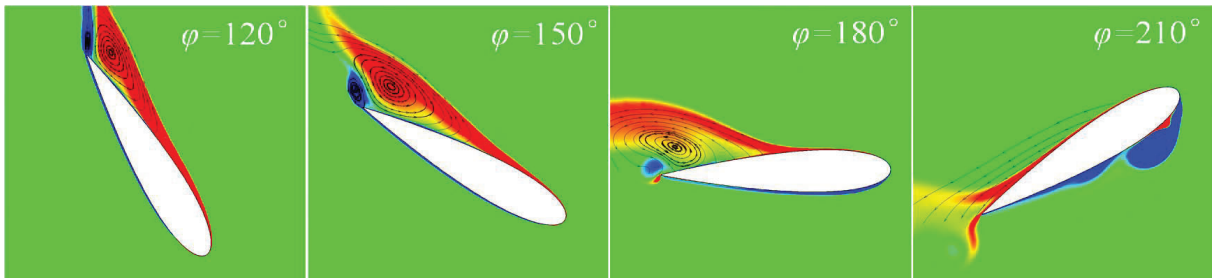
a. Clean blade

b. Flap 7520

c. Flap 7510
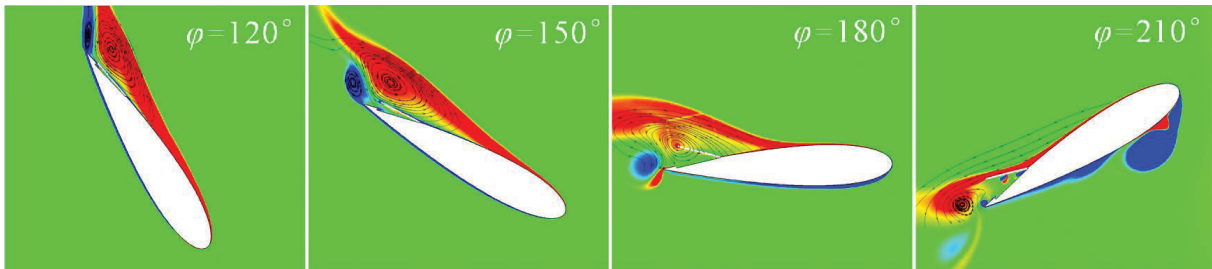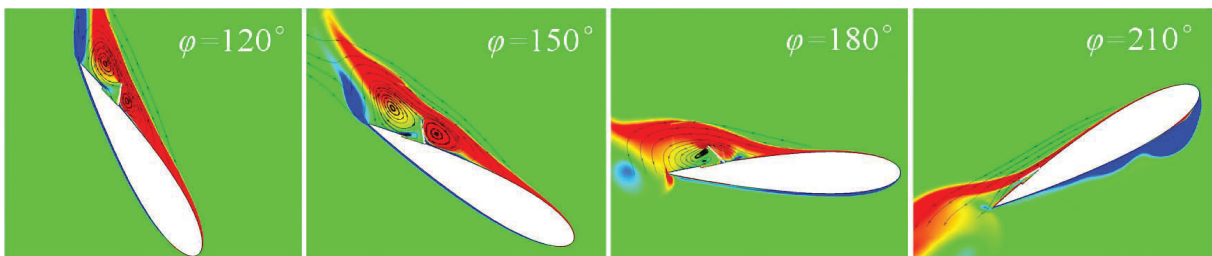
Z Vorticity: -500   -400   -300   -200   -100   0   100   200   300   400   500
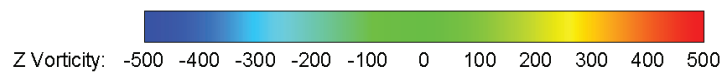
1   Fig. 12. Vorticity contour and relative velocity streamlines of the clean blade and flap blades

2   (TSR=1.5)

3   To further explore the relationship between the flap-fluid interaction and the blade torque, it is

4   necessary to deeply analyze the blade lift and drag coefficients. Without considering the influence

5   of flow induction, combined with Fig. 3, the blade AoA (α) under different TSRs (λ) and azimuth

6   angles (φ) can be derived by the following equation:

7    $$\alpha = \arctan\left(\frac{\sin\varphi}{\lambda + \cos\varphi}\right)$$ (4)

8   Meanwhile, the relative wind velocity received by the blade can also be obtained by using

9   Equation (5).

10    $$V_{rel} = V\sqrt{\sin^2\varphi + (\lambda + \cos\varphi)^2}$$ (5)

11   Then, the lift coefficient and drag coefficient can be derived by Equation (6) and Equation (7)

12   respectively based on the calculated tangential force and radial force.

13    $$C_L = \frac{F_n\cos\alpha + F_t\sin\alpha}{1/2\rho V_{rel}^2 ch}$$ (6)

14    $$C_D = \frac{F_n\sin\alpha - F_t\cos\alpha}{1/2\rho V_{rel}^2 ch}$$ (7)

15   Fig. 13 shows the AoAs and the corresponding lift and drag coefficients at the key azimuth

16   angles by considering Flap 7510. From the figure, it can be seen that Flap 7510 increases the lift

17   coefficient and decreases the drag coefficient at the azimuth angles of 120° and 150°, respectively,

18   which corresponds to an increase above the blade rotational torque. At the azimuth angle of 180°

19   with the AoA of 0°, the lift coefficient does not contribute to the blade rotation torque. The flap

20   leads to an increase in the drag coefficient, which results in the decrease in the blade rotational

1 torque. At an azimuth of 210°, the flap has almost retracted to the blade surface, so the lift and drag

2 coefficients are not significantly affected.
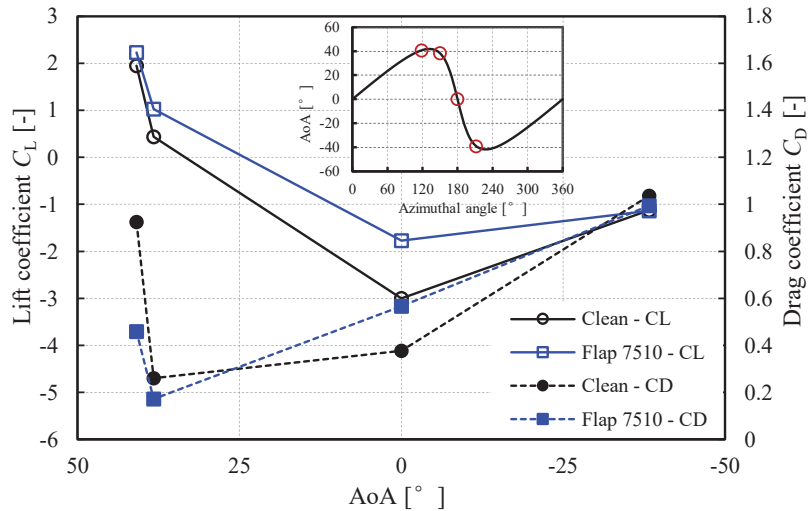
3

4 Fig. 13. AoAs and the corresponding lift and drag coefficients at the key azimuth angles

5 considering Flap 7510 (TSR=1.5)

6 The pressure distribution around Flap 7510 at the key azimuth angles is also shown in Fig. 14.

7 From the figures, it is observed that when the flap is blocking the backflow generated from the flow

8 separation (at the azimuth angle of 120° and 150°, respectively), a high-pressure area is generated

9 on the upstream side (flap left side) and a low-pressure area is generated on the downstream side

10 (flap right side). This high-pressure area not only increases the pressure near the blade trailing edge

11 but also increases the pressure on the opposite side of the blade resulting in an increase in pressure

12 difference on both sides of the blade, so as to enhance the lift coefficient and reduce the drag

13 coefficient. However, when the flow tends to the attached state (at the azimuth angle of 180°), a

14 high-pressure area is generated on the right side of the flap as the flap is blocking the main flow.

15 This is, opposite to the above situation, resulting in a reduction of the lift coefficient and an increase

16 in the drag coefficient. Although Flap 7510 shows both positive and negative effects in the whole

1   process, it is generally found to offer beneficial effects in improving the power coefficient of the

2   VAWT because of its quick reaction and sustained effort in blocking the backflow.

3

4   a. $\varphi=120°$ b. $\varphi=150°$

5

6   c. $\varphi=180°$ d. $\varphi=210°$
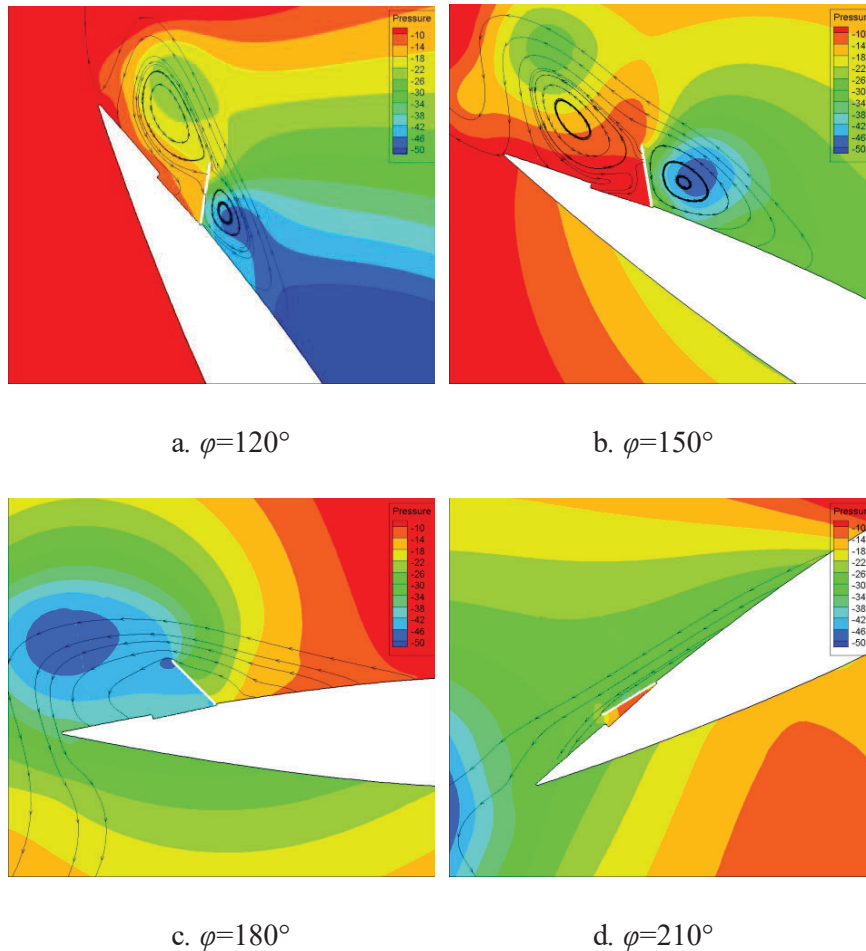
7   Fig. 14. Pressure distribution around Flap 7510 at the key azimuth angles (TSR=1.5)

8   *3.2. Flow control effect of flaps at different locations*

9   The shorter flap is more responsive, hence the flaps with the length of $0.1c$ are installed on the

10   inner sides of the blades $0.75c$ (Flap 7510), $0.58c$ (Flap 5810), and $0.40c$ (Flap 4010) from the BLE,

11   respectively. The flow control effect of flaps at different locations are studied. The power

12   coefficients of the clean VAWT and the flap VAWTs are shown in Fig. 15. When the TSR is high

13   (TSR=1.5), the closer the flap is to the BLE, the worse is its flow control effect. Therefore, Flap

1   5810 and Flap 4010 both result in negative effects as reflected by their lower power coefficients.

2   However, for the lower TSRs of 0.6 and 0.9, the effects of flow control from Flap 5810 and Flap

3   4010 are both positive and even better than that of Flap 7510. Additionally, compared with the

4   clean VAWT, Flap 4010 leads to the greatest power coefficient increase with a value of 0.058 at the

5   TSR of 0.9. This is followed by Flap 5810 with the highest power rate coefficient increase of 89.1%

6   at the TSR of 0.6. The overall trend shows that the closer the flap is to the BLE, the better the

7   performance is at low TSRs. However, it should be noted that the forward-most flap (Flap 4010)

8   shows a weaker performance than that of Flap 5810 at a TSR of 0.6.
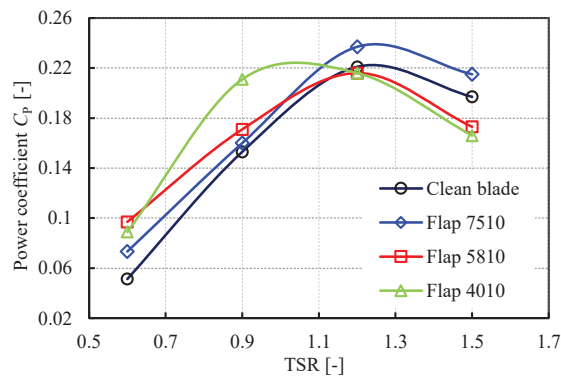
9

10   Fig. 15. Power coefficients of VAWTs with different flap locations

11   To further analyze the control effect of the flaps and clarify the influence of the flap location,

12   the blade torques and flap angles with Flap 5810 and Flap 4010 respectively versus the azimuth

13   angle at the TSR of 0.6 are shown in Fig. 16. It can be seen from the plots that the blade torque is

14   significantly increased by both flaps between azimuth angles of about 70° and 130°. Meanwhile,

15   the increased blade torques both experienced sudden surge at a high frequency near the beginning

16   of the peak values. This is associated with the vibrations of the flaps caused by the interaction of the

17   artificial reverse torque and the aerodynamic force when the flaps reached their upper rotational

1 limit.

2   By comparing the blade torques with Flap 5810 and Flap 4010, it is found that although Flap

3 5810 is covered by the flow separation earlier (because the transition in flow separation

4 development is from the BTE to the BLE) and thus has the priority to be raised, its blade torque

5 does not increased earlier. From the curves of the flap angle, when Flap 5810 just reaches the upper

6 rotational limit, it drops and then suddenly rises again. Therefore, although Flap 4010 rises later, it

7 stabilizes at the upper rotational limit earlier, resulting in the blade torque being enhanced earlier.

8 However, when the azimuth angle is greater than 90°, the blade torque with Flap 4010 reduces

9 faster than that of Flap 5810, which makes the power coefficient lower than that of Flap 5810 as

10 shown in Fig.15. Furthermore, between the azimuth angles of 120° ~ 130°, the blade torque with

11 Flap 4010 decreases significantly, corresponding to the rapid retraction shown by the flap angle

12 plots. It should be noted that the flaps at the above two locations both deploy and retract twice in a

13 revolution, which is different from Flap 7520 and Flap 7510 that only perform (deploy and retract)

14 once at high TSR.
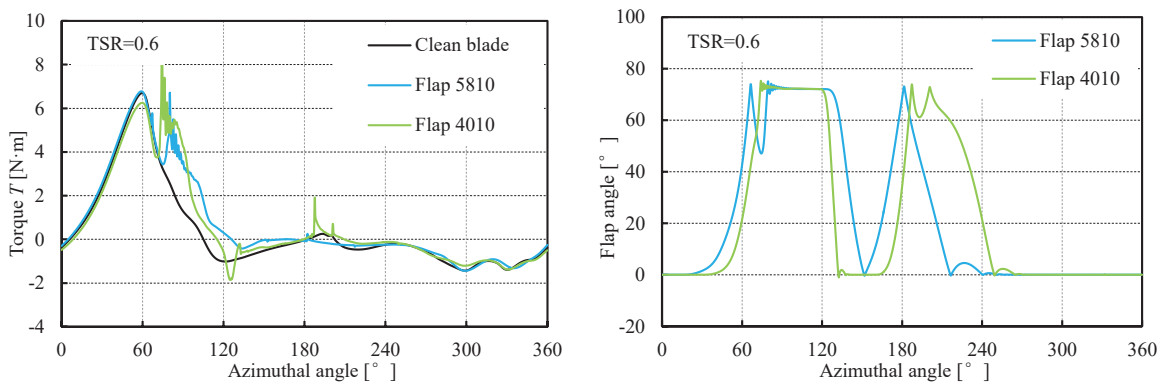
15

16   a. blade torques   b. flap angles

17 Fig. 16. Blade torques and flap angles with Flap 5810 and Flap 4010 versus the azimuth angle at the

1   TSR of 0.6

2   By selecting critical azimuth angles, Fig. 17 shows the vorticity contour and relative velocity

3   streamlines around the blades with Flap 5810 and Flap 4010 at the TSR of 0.6. It can be seen that

4   the flow separation near the BTE has occurred on the inner side of the blade at an azimuth angle of

5   60°, and the two flaps are both raised by the separation backflow with Flap 5810 getting a higher

6   flap angle. When the blade moves to an azimuth angle of 75°, the BLE flow separation occurs. Flap

7   5810 cannot effectively block the backflow induced by the BLE flow separation due to its

8   backward location. Meanwhile, Flap 4010 plays a role in stably blocking the backflow, resulting in

9   a vortex formed on the lee side of the flap. Because of the blocking effect, the size of the BLE

10   vortex is reduced and the blade torque is increased.

11   At an azimuth angle of 120°, due to the low TSR, the BLE vortex moves towards the right side

12   of the blade after shedding, and a new reverse vortex is formed from the incoming flow at the BTE.

13   As the reverse vortex is formed close to the blade surface, which may be affected by the blocking of

14   the BLE vortex in the previous stage, there is no backflow from the BTE to the BLE near Flap 4010.

15   Therefore, Flap 4010 cannot continue to block the backflow from the BLE flow separation. In the

16   case of Flap 5810, the reverse vortex is further away from the blade surface, so the flow around the

17   flap is still controlled by the BLE vortex and the backflow from the BLE flow separation can be

18   blocked. This is the main reason why Flap 5810 performs better.

19   When the azimuth angle reaches 135°, the flaps at both locations are covered by the reverse

20   vortices, causing the fluid near the flaps to flow towards the BTE, which drives the flaps to retract.

21   At an azimuth angle of 180°, the reverse vortices develop further and are both close to the front part

of the blade's upper surface. Under the impact of the inflow from the BTE, both flaps rise again, but

due to the presence of the reverse vortices, the two flaps fail to block the countercurrent flow.

Overall, at the low TSR, although the forward Flap 4010 blocks the BLE vortex better, the

blocking causes the reverse vortex formed near the BTE to be close to the flap. This causes the flap

to lose its controllability, resulting in a weaker performance than that of the backward Flap 5810.

a. Flap 5810

b. Flap 4010

Z Vorticity: -200 -160 -120 -80 -40 0 40 80 120 160 200
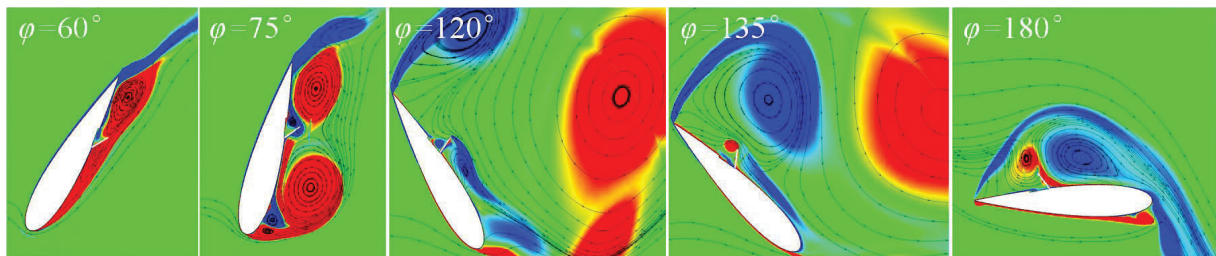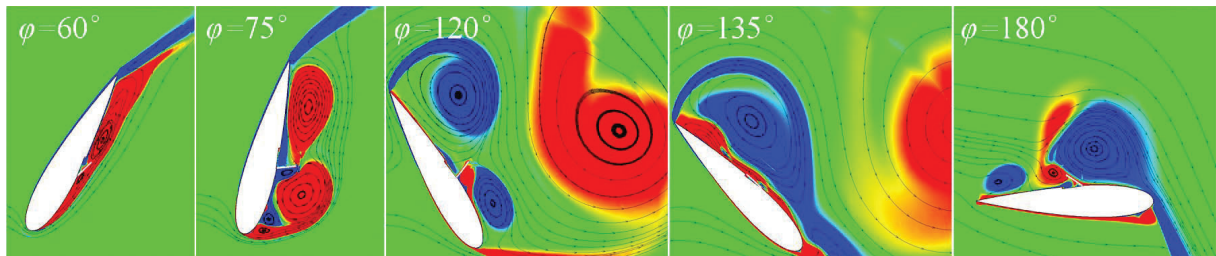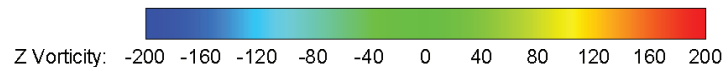
Fig. 17. Vorticity contour and relative velocity streamlines around the blades with Flap 5810 and

Flap 4010 (TSR=0.6)

3.3. Flow control effect of flaps installed on both sides of the blades

When analyzing the flap installed on the inner side of the blade, it is found that in the

downwind region, the blade torque is usually negative due to flow separation on the outer side of

the blade. This is one of the reasons why it is necessary to study the flow control effect when the

1   flaps are installed on the inner and outer sides of the blade. Fig. 18 shows the power coefficients

2   from the clean VAWT and the VAWTs with Flap 7510 installed on the inner side only and on both

3   sides of the blade respectively. It can be seen that the power coefficient has been significantly

4   improved by the flaps installed on both sides of the blade, especially at high TSRs. The power

5   coefficient is increased by 29.9% at the TSR of 1.5. For comparison, the flap installed on the inner

6   side only provided an increase in power coefficient of 9.1% in this scenario.

7   Fig. 19 shows the torques of the clean blade and blades with Flap 7510 installed on the inner

8   side only and on both sides of the blade at the TSR of 1.5. As shown in the figure, the torque curve

9   for the flaps installed on both sides almost coincides with that of the flap only installed on the inner

10   side at azimuth angle range of 120° ~ 240°. The flow separation mainly occurs on the inner side,

11   and the outer flap remains attached to the blade. When the azimuth angle is greater than 240°, the

12   flow separation occurs on the outer side and the outer flap works to increase the blade torque

13   significantly, indicating that the outer flap plays a positive role in controlling the flow separation.

14   From the flow field around the outer flap shown in Fig. 20, a large flow separation vortex appears

15   on the outer side of the blade at azimuth angle of 270°. At this time, although the outer flap is raised,

16   only a slight blocking effect to the separation backflow is observed. At azimuth angles of 300° and

17   330°, the outer flap obviously blocks the separation backflow with a vortex established on the lee

18   side of the flap. When the blade reaches azimuth angle of 360°, the flow tends to be attached, and

19   the outer flap begins to retract to the blade surface under the impact of the mainstream flow.

20   From Fig.18, it can be seen that the control effect on both sides of the installation is not

21   significantly better than that of the inner side installation at a TSR of 0.6. To clarify this, Fig. 21

1   shows the flow field around the outer flap at different azimuth angles in the downwind region. Due

2   to the complexity of the flow evolution and flap motion, the flow field is shown at every 15° of the

3   azimuth angle. From the figure, the flap only has the qualification or the tendency to block the

4   backflow at azimuth angles of 195°, 270°, and 330° where the fluid near the flap flows from the

5   BTE to the BLE. However, due to the influence of vortices formed near the BTE, the blocking

6   effect of the flap cannot be sustained, thereby causing the outer flap to fail to achieve an effective

7   flow control measures.
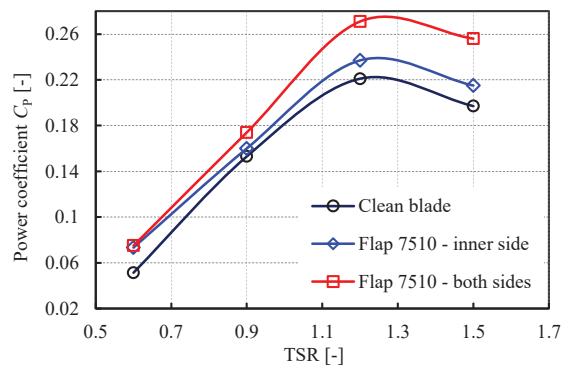
8

9   Fig. 18. Power coefficients of the clean VAWT and the VAWTs with Flap 7510 installed on the

10   inner side only and on both sides of the blade respectively
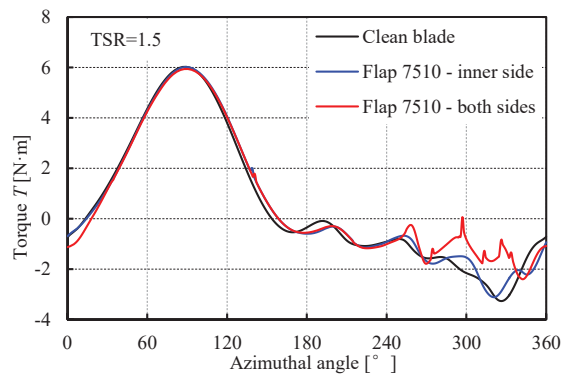
11

12   Fig. 19. Torques of the clean blade and blades with Flap 7510 installed on the inner side only and

13   on both sides of the blade respectively at the TSR of 1.5

a. *φ=270°* b. *φ=300°* c. *φ=330°* d. *φ=360°*

Z Vorticity: -500 -400 -300 -200 -100 0 100 200 300 400 500
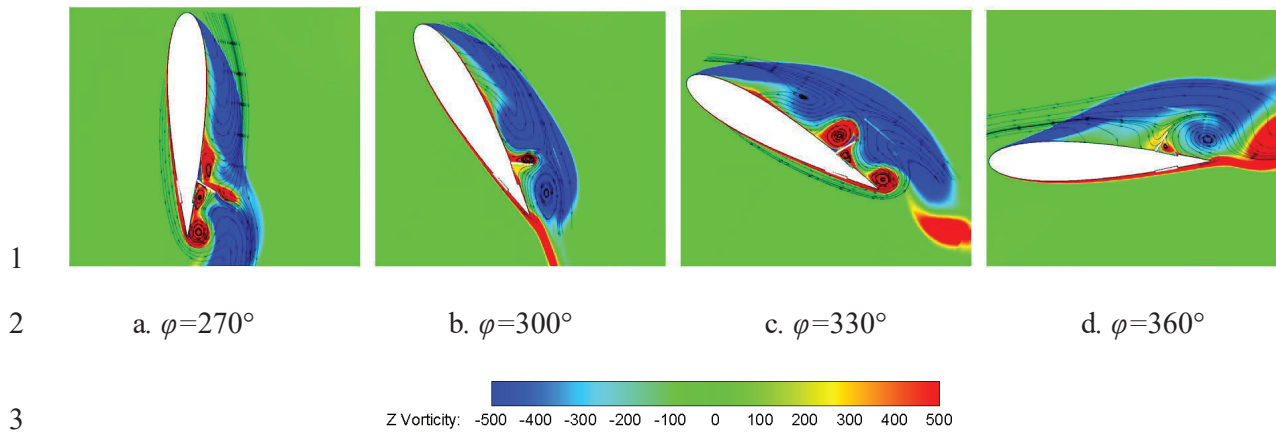
Fig. 20. Flow field around the outer flap at the TSR of 1.5

φ=180° *φ=195°* *φ=210°* *φ=225°* *φ=240°* *φ=255°* *φ=270°*

φ=285° *φ=300°* *φ=315°* *φ=330°* *φ=345°* *φ=360°*

Z Vorticity: -200 -160 -120 -80 -40 0 40 80 120 160 200
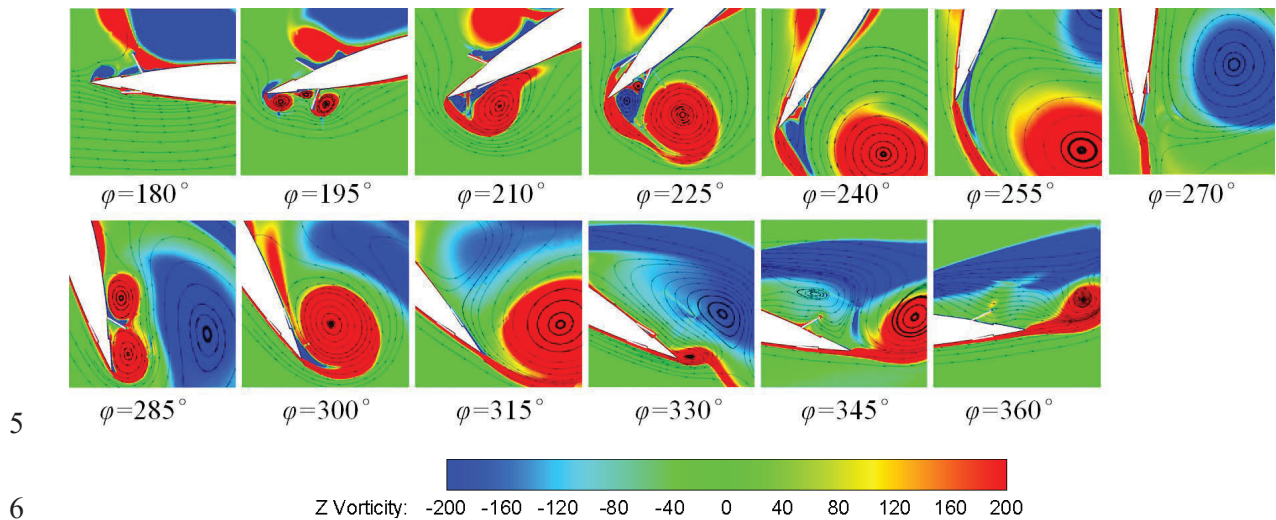
Fig. 21. Flow field around the outer flap at a TSR of 0.6

4. Discussions

The adaptive flap is a movable flow control component that depends on the flow state. For example, understanding the negative effect caused by Flap 7520 at a high TSR of 1.5 is critical to its application as an adaptive flap for flow control. Due to the rapid change in the flow field, it is observed that Flap 7520 is incapable of raising instantaneously when the flow separation occurs and cannot equally retract in time when the flow tends to the attachment state. The delayed flap retraction causes the flap to obstruct the main flow from attaching to the blade surface and thus,

1   reduces the aerodynamic torque of the blade. This obstruction cannot be avoided because the flap

2   needs the driving force caused by the obstruction in order to retract. Therefore, maneuverability of

3   the flap is the primary problem experienced by adaptive flap in flow control, which needs urgent

4   solution in order to facilitate its application in VAWT that is known to suffer from intermittent flow

5   separation problem. Improving the adaptive flap's maneuverability can mitigate the delayed raise

6   and retraction of the flap in flow control.

7   A direct way to improve the flap's maneuverability is by altering the flap length as it is found

8   that reducing the flap length offers the most effective solution to flap maneuverability. The results

9   of an investigation on a shorter flap show that when the flow separation occurs, the flap is raised

10   quickly under the action of the backflow and then increases the blade torque by blocking the

11   backflow. When the flow tends to the attachment state, the flap is found to instantaneously retract to

12   the blade surface. Therefore, the shorter flap provides a positive effect in the whole range of TSR

13   and different flow patterns. The shorter flap shows the superiority of adaptive flap compared with

14   other conventional passive control technologies such as vortex generators which only works in

15   weak flow separation conditions [7] and leading-edge serrations whose obvious effect only exists in

16   a narrow range of TSR [8]. Certainly, there are other methods that can be used to improve the flap's

17   maneuverability, like those that work by reducing the moment of inertia of the flap or adding a

18   magnetic auxiliary device. Taking the magnetic auxiliary device as an example, a repulsive

19   magnetic force near the blade surface will be activated to drive the flap to rise when the flow

20   separation is detected. When the flow attachment is detected, an attractive magnetic force will be

21   activated to cause the flap to retract in time to aid the maneuverability. The required flow separation

1   detection can be achieved by installing a micro adaptive flap at a suitable location.

2   When a short flap moves towards the BLE, a negative effect occurs at a high TSR. This is

3   because the closer the location is to the BLE, the faster the local flow state changes, that is, the less

4   time it takes for the flow to separate and then reattach as the flow separation generally tends to

5   spread from the BTE to the BLE and disappears gradually in the opposite direction. Therefore, even

6   for the short flap, its mobility could occasionally be hindered by poor maneuverability. However,

7   any flap located closer to the BLE generally has the potential to provide better effects at low TSR.

8   This is because of its better ability in blocking the backflow caused by the BLE flow separation,

9   although the flap generally cannot continuously block the backflow with the interference by the

10 reverse vortices from the BTE. The reverse vortices also help to explain the phenomenon that the

11 effect of Flap 4010 is weaker than that of Flap 5810 at the TSR of 0.6.

12   Compared with the inner flap, the flow control effect of the flaps on both sides of the blade is

13 more competitive, especially at high TSRs of 1.2 and 1.5. This is due to the mitigation provided by

14 the outer flap on the flow separation outside of the blade and in the downwind region. This is

15 reflected by the formation of vortex on the lee side of the flap caused by the backflow blocking.

16 However, at the low TSR of 0.6, the outer flap does not play any significant role in the flow control.

17 It is found that the flap is either attached or in a rotating state, in most cases, without the persistent

18 backflow blocking due to the influence of the vortices formed near the BTE.

19   It is found that the problem of flow separation in VAWT at low TSRs is characterized by the

20 BLE flow separation and accompanied by the BTE vortices. When the BLE vortices are shed at far

21 away from the blade, the BTE vortices are drawn closer to the blade, resulting in a flow near the

flap and towards the BTE. This drives the flap to attach to the blade and makes it impossible for the

flap to continuously control the BLE flow separation.

The high-solidity VAWT is the focus of the present work. However, for the scenario of low

and moderate solidity VAWT, the adaptive flap also has a great application prospect and is worth

further discussion. Findings from this research indicate that the flow separation forms on VAWT

can be classified into trailing-edge flow separation at high TSR and leading-edge flow separation at

low TSR. The evolution of the trailing-edge flow separation mainly follows the rotation of the wind

turbine and occurs at a higher TSR for low and moderate solidity VAWT than that for the high

solidity VAWT. Therefore, when the low solidity of VAWT is realized by reducing the number of

the blades, the flap may face the challenge of insufficient maneuverability. However, when the low

solidity VAWT is obtained by reducing the blade chord length, the flap gets asynchronously

reduced in size and can deal with the change of flow state faster. The evolution of the leading-edge

flow separation is characterized by alternating the shedding of the leading-edge vortices and

trailing-edge vortices, which is similar to Carmen Vortex Street, so the evolution frequency is

mainly affected by the blade chord length. For the low and moderate solidity VAWT with a shorter

blade chord, the evolution frequency of the leading-edge flow separation is higher, but the flap size

is smaller, so the flap's maneuverability needs to be confirmed in combination with specific

situations.

5. Conclusions

In order to comprehensively investigate the performance of an adaptive flap in mitigating the

flow separation problem in VAWT and explore the flow control mechanism, adaptive flaps are

installed on a high-solidity VAWT by considering different lengths and locations and then studied

using CFD in combination with FSI algorithm. The results of the flap installed on the inner side of

the blade show that longer flap faces a problem of insufficient maneuverability and causes a

negative effect at the high TSR. On the other hand, the shorter flap alleviates this problem and

increases the blade torque by blocking the backflow, thus offering a positive flow control effect in

the whole range of TSRs. This finding reflects the advantages offered by the adaptive flap to

different flow patterns. In addition, for the shorter flap located closer to the BLE, the negative effect

occurs at the high TSR because the flow separation and attachment change is faster than in other

configurations. Notwithstanding, the forward flap generally offers a better performance at the low

TSR due to the superior capability in blocking the backflow caused by BLE flow separation.

The results of the flaps installed on both sides of the blade show that their performance is more

competitive. This is because the flow control is also required to guarantee separation on the outer

side of the blade, which is especially evident at a high TSR of 1.5 where the power rate coefficient

increase is 29.9%, i.e. three times that of the flap installed on the inner side only. Regardless of

whether it is the inner or the outer flap, control processes at low TSRs are found to be complicated

and their performances are usually weakened. This is because the typical BTE vortices at low TSRs

suppresses the rise of the flap, making it unable to continuously mitigate the BLE flow separation.

Acknowledgment

1   University Capacity Building Project (grand number: 19060502200).

2   **References**

[1]   Hand B, Cashman A. A review on the historical development of the lift-type vertical axis wind turbine: From onshore to offshore floating application [J]. Sustainable Energy Technologies and Assessments, 2020, 38:100646.

[2]   Greenblatt D, Harav A B, Mueller-Vahl H. Mechanism of Dynamic Stall Control on a Vertical Axis Wind Turbine[C]// 51th AIAA Aerospace Sciences Meeting Including the New Horizons Forum & Aerospace Exlocation, USA, 2013.

[3]   Elsakka M M, Ingham D B, Ma L, Pourkashanian, M. CFD analysis of the angle of attack for a vertical axis wind turbine blade [J]. Energy Conversion and Management, 2019, 182:154-165.

[4]   McConnell RD. Giromill overview [R]. United States: Wind energy innovative systems conference, 1979.

[5]   Xu Y, Peng Y, Zhan S. Optimal blade pitch function and control device for high-solidity straight-bladed vertical axis wind turbines [J]. Applied Energy, 2019, 242:1613-1625.

[6]   Gad-El-Hak M. Flow control: Passive, Active, and Reactive Flow Management [M]. Cambridge University Press, London, 2000.

[7]   Yan Y, Avital E, Williams J, Cui J. CFD analysis for the performance of microvortex generator on aerofoil and vertical axis turbine [J]. J. Renewable Sustainable Energy, 2019, 11, 043302.

[8]   Wang Z, Wang Y, Zhuang M. Improvement of the aerodynamic performance of vertical axis wind turbineswith leading-edge serrations and helical blades using CFD and Taguchi method [J]. Energy Conversion and Management, 2018, 177: 107-121.

[9]   Mohamed OS, Ibrahim AA, Etman AK, Abdelkader A, Elbaz A. Numerical investigation of

Darrieus wind turbine with slotted airfoil blades [J]. Energy Conversion and Management: X, 2020, 5: 100026.

[10] Bechert D, Bruse M, Hage W, Meyer R. Biological surfaces and their technological application - Laboratory and flight experiments on drag reduction and separation control [C]// AIAA 28th Fluid Dynamics Conference, Snowmass Village, Co, USA, 1997.

[11] Meyer R, Hage W, Bechert D W. Separation Control by Self-Activated Movable Flaps [J]. AIAA Journal, 2007, Vol. 45(1):191-199.

[12] Patone G, Muller W. Aeroflexible Oberflächenklappen als "Rückstrombremsen" nach dem Vorbild der Deckfedern des Vogelflügels [R]. Technical Report TR-96–05, Technical University Berlin, 1996.

[13] Bramesfeld G, Maughmer M. Experimental Investigation of Self-Actuating, Upper-Surface, High-Lift-Enhancing Effectors [J]. Journal of Aircraft, 2002, 39(1):120-124.

[14] Kernstine K, Moore C, Cutler A, Mittal R. Initial Characterization of Self-Activated Movable Flaps, "Pop-Up Feathers" [C] // 46th AIAA Aerospace Sciences Meeting and Exhibit, Reno, Nevada, USA, 2008.

[15] Allemand G and Altman A. Post-Stall Performance Improvement through Bio-inspired Passive Covert Feathers [C] // 54th AIAA Aerospace Sciences Meeting, San Diego, California, USA, 2016.

[16] Wang C H, Schlüter J. Stall control with feathers: Self-activated flaps on finite wings at low Reynolds numbers [J]. Comptes rendus - Mécanique, 2012, 340(1):57-66.

[17] Arivoli D, Singh I. Self-adaptive flaps on low aspect ratio wings at low Reynolds numbers[J]. Aerospace Science & Technology, 2016, 59:78-93.

[18] Schatz M, Bunge U, Lübcke H, Thiele F. Numerical Study of Separation Control by Movable Flaps [J]. Notes on Numerical Fluid Mechanics, Springer, 2001.

[19] Hao W, Li C. Performance improvement of adaptive flap on flow separation control and its effect on VAWT [J]. Energy, 2020, 213: 118809.

[20] Peng H Y, Lam H F, Liu H J. Power performance assessment of H-rotor vertical axis wind turbines with different aspect ratios in turbulent flows via experiments [J]. Energy, 2019, 173: 121-132.

[21] McLaren K, Tullis S, Ziada S. Computational fluid dynamics simulation of the aerodynamics of a high solidity, small scale vertical axis wind turbine [J]. Wind Energy, 2012, 15(3):349-61.

[22] Timmer WA. Two-dimensional low-Reynolds number wind tunnel results for airfoil NACA0018 [J]. Wind Engineering, 2009, 32(6): 525-537.

[23] Elkhoury M, Kiwata T, Aoun E. Experimental and numerical investigation of a three-dimensional vertical-axis wind turbine with variable-pitch [J]. Journal of Wind Engineering and Industrial Aerodynamics, 2015, 139: 111-123.

[24] Wang D, Dong S, Ning M, Incecik A. Extended variable-time-step Adams–Bashforth–Moulton method for strongly coupled fluid–structure interaction simulation [J]. Ocean Engineering, 2020, 219:108335.

[25] Larose GL, Auteuil AD. Effect of local air compressibility on the aerodynamics of rectangular prisms at Mach number below 0.3 [C] // 6th International Colloquium on: Bluff Bodies Aerodynamics & Applications. Milano, Italy, 2008.

[26] Zanforlin S, Deluca S. Effects of the Reynolds number and the tip losses on the optimal aspect ratio of straight-bladed Vertical Axis Wind Turbines[J]. Energy, 2018, 148: 179-195.

[27] Menter FR, Two-Equation Eddy-Viscosity Turbulence Models for Engineering Applications [J]. AIAA Journal, 1994, 32 (8):1598-605.

[28] Wilcox DC. Reassessment of the scale-determining equation for advanced turbulence models [J]. AIAA Journal, 1988, 26: 1299-1310.

[29] Jones WP, Launder BE. The calculation of low-Reynolds-number phenomena with a two-equation model of turbulence [J]. International Journal of Heat And Mass Transfer, 1972, 16: 1119-1130

[30] Daroczy L, Janiga G, Petrasch K, Webner M, Thévenin D. Comparative analysis of turbulence models for the aerodynamic simulation of H-Darrieus rotors [J]. Energy, 2015, 90: 680-690.

[31] Tezduyar T E. Stabilized Finite Element Formulations for Incompressible Flow Computations [J]. Advances in Applied Mechanics, 1991, 28(28): 1-44.

[32] Rezaeiha A, Kalkman I, Blocken B. CFD simulation of a vertical axis wind turbine operating at a moderate tip speed ratio: guidelines for minimum domain size and azimuthal increment [J]. Renewable Energy 2017; 107: 373-85.

[33] Edwards JM, Danao LA, Howell RJ. PIV measurements and CFD simulation of the performance and flow physics and of a small-scale vertical axis wind turbine [J]. Wind Energy 2015; 1: 201-17.

[34] Ma N, Lei H, Han Z, Zhou D, Bao Y, Zhang K, Zhou L, Chen C. Airfoil optimization to improve power performance of a high-solidity vertical axis wind turbine at a moderate tip speed ratio [J]. Energy, 2018, 150: 236-252.

[35] Li C, Zhu S, Xu Y, Xiao Y. 2.5D large eddy simulation of vertical axis wind turbine in consideration of high angle of attack flow [J]. Renewable Energy, 2013, 51: 317-330.